Improving Performance of Integrated Ground-HAPS FSO Communication Links With MIMO Application

Emna Zedini ⓘ, *Member, IEEE*, Yalçın Ata ⓘ *, Senior Member, IEEE*, and Mohamed-Slim Alouini ⓘ *, Fellow, IEEE*

Abstract—In this paper, we investigate the performance of multiple-input multiple-output (MIMO) free-space optical (FSO) communication systems, encompassing both slant path (down-link and uplink) and horizontal links. The FSO links span ground-to-high altitude platform system (HAPS), HAPS-to-ground, and HAPS-to-HAPS configurations. To model the atmospheric turbulence-induced fading, pointing error impairments, and angle-of-arrival (AOA) fluctuations, we employ the Gamma-Gamma distribution, Hoyt distribution, and Rayleigh distribution, respectively. We then derive the probability density function (PDF) of the end-to-end signal-to-noise ratio (SNR) under the combined effect of turbulence, AOA fluctuations, attenuation due to absorption and scattering, and generalized pointing error impairments. Capitalizing on this PDF expression, we present novel results for fundamental performance metrics, including outage probability, average bit-error rate (BER) of on-off keying (OOK) modulation scheme, and ergodic capacity expressed in terms of the Meijer's G function. Additionally, we provide highly accurate asymptotic results for the outage probability and the average BER at high SNR, obtained in terms of simpler functions. Furthermore, we demonstrate that the integration of MIMO configurations in either the transmitter, receiver, or both significantly enhances the performance of FSO communication links. To validate our analytical results, computer-based Monte-Carlo simulations are conducted, affirming the reliability of our findings.

Index Terms—Free-space optics (FSO), multiple-input multiple output (MIMO), optical wireless communication, slant path communication, spatial diversity technique.

I. INTRODUCTION

OVER the past decade, there has been a growing interest in the use of high altitude platform system (HAPS) to enhance the performance of free-space optical (FSO) communication systems. This approach has emerged as a promising alternative to sustain FSO communication link connectivity and ensure reliable communication. HAPSs are utilized for non-line-of-sight (NLoS) communication, acting as relays to enhance performance and coverage. They are cost-effective and easily deployed, finding applications in various industries like disaster monitoring, emergency communication, agriculture, environmental monitoring, surveillance, internet connectivity, and broadcasting. Consequently, significant efforts have been directed towards investigating the performance of HAPS-based FSO communication systems across various aspects [1], [2], [3], [4], [5], [6], [7]. In [1] and [2], the reliability, link availability and outage performance of HAPS assisted FSO link was analyzed and it was shown that the multi-hop HAPS FSO communication mitigates the channel fading effects significantly. Basic networking architectures and design considerations were discussed in [3] in terms of size, weight, power, and endurance capability constraints. The variation of the optimal altitude of HAPSs to avoid interference together with the number of HAPSs was analyzed in [4]. A detailed analysis of the outage performance for uplink HAPS FSO was investigated in various aspects and an optimization of the transmitted laser beam and the field-of-view (FoV) of the receiver was studied to provide minimum error probability in [5]. Then an extended study was performed [6] by adding average bit-error-rate (BER) and ergodic capacity and the performance optimization by properly designing the angle of FoV, the receiver aperture size, and the beam divergence angle was emphasized. The hybrid radio frequency (RF)-FSO ground-satellite communication through HAPS relay was also investigated in [8] and it was shown that the selection of HAPS enhances the performance of ground-satellite link remarkably. In [9], by deploying a HAPS relay above the ground station, a significant mitigation in the effects of the atmospheric turbulence was observed and a high-performance FSO transmission between ground station and satellite through the HAPS relay was achieved, regardless of the zenith angle of the satellite. While the above mentioned studies indicate that FSO communication systems experience performance improvements with HAPS-assisted links, turbulence-induced fading and environmental conditions remain significant factors limiting the overall performance of these systems. Addressing these challenges is essential to further enhance the reliability of FSO communication in HAPS-integrated setups.

To counter the detrimental impact of atmospheric turbulence on the performance of FSO communication systems, various mitigation techniques have been employed. These include aperture averaging, multiple-input multiple-output (MIMO), and adaptive optics (AO) correction, which have been applied to different FSO communication systems. The effectiveness of aperture averaging in enhancing the performance HAPS-assisted FSO communication was assessed in [8]. Another significant

turbulence mitigation technique, AO correction, was explored in [7], revealing its positive impact up to a certain extent. Additionally, [10] reported an improvement in the performance of laser communication systems with AO correction, showcasing a reduction in the BER for downlink, uplink, and horizontal link configurations.

A. MIMO Background

In addition to aperture averaging and adaptive optics correction, spatial diversity emerges as another beneficial technique to improve the performance of FSO communication systems. Employing multiple transmitters and receivers that are mounted to offer statistically independent fading channels, the application of MIMO configurations has demonstrated notable power and performance gains in the presence of atmospheric turbulence. This enhancement has been substantiated both theoretically and experimentally [11]. The work presented in [12] investigated the mitigation of atmospheric turbulence effects in FSO systems utilizing multiple receiver apertures, specifically in Log-normal distributed fading channels for both on-off keying (OOK) and subcarrier intensity modulation (SIM). Furthermore, the study conducted in [12] established that maximum ratio combining (MRC) spatial diversity combining technique exhibits superior performance compared to equal gain combining (EGC) and selective combining (SelC) techniques, which show decreasing levels of effectiveness, respectively.

The impact of atmospheric turbulence characterized by a Log-normal distribution on a MIMO FSO link using multiple laser transmitters and multiple avalanche photodetector (APD) photodetectors was investigated in [13]. Analytical performance bounds were obtained under Q-ary pulse position modulation (PPM) and EGC technique. In [14], various modulation schemes, such as OOK, differential quadrature phase-shift keying (DQPSK), and differential phase-shift keying (DPSK) were investigated for two different receiver aperture scenarios in Gamma-Gamma distributed atmospheric turbulence channels. The performance analysis of a MIMO FSO communication system utilizing intensity-modulation direct-detection (IM/DD) scheme with MRC and EGC techniques, was conducted in [15]. The study focused on a Gamma-Gamma distributed turbulence channel and addressed stability challenges at high SNR by employing a generalized infinite power series. The variation of BER and SNR for a MIMO FSO communication system utilizing SIM phase-shift keying (PSK) modulation scheme and considering both repetition and Alamouti codes was given in Gamma-Gamma distributed atmospheric turbulence channel [16]. The study in [17] investigated the BER performance for a binary phase-shift keying (BPSK) modulated FSO communication system. The analysis considered negative exponential distributed atmospheric turbulence and highlighted the advantages of employing multiple receiver apertures. The results indicated that the MRC technique outperformed EGC and SelC techniques, in the presence of both non-Gaussian noise and additive white Gaussian noise (AWGN). The work in [18] explored the performance of a M-ary phase-shift keying (MPSK) modulation scheme in a MIMO FSO communication link, considering the Malaga atmospheric turbulence channel. The study demonstrated a substantial reduction in the average BER with an increase in the number of transmit and receive apertures. The combined effect of Gamma-Gamma distributed atmospheric turbulence and attenuation (caused by drizzle, haze, fog etc.) on FSO communication system with multiple receivers was examined in [19] and BER reduction with the increased number of receivers was shown. Authors in [19] extended their work for MIMO FSO communication links, including attenuation and Gamma-Gamma distributed turbulence channel effects [20].

In [21], the study combined the impact of misalignment, modeled by Gaussian distribution, with the negative exponential distributed turbulent fading channel. The research focused on analyzing the outage performance of a horizontal MIMO FSO communication link employing IM/DD scheme. The findings indicated a noteworthy performance improvement when using EGC. The impact of pointing errors and atmospheric turbulence on the performance of OOK and BPSK modulated FSO communication systems having multiple receiver apertures was investigated using Gamma-Gamma [22] as well as Log-normal distributed fading channel models [23]. In [24], the effect of Gaussian distributed pointing errors in Gamma-Gamma turbulent channels was examined for MIMO FSO systems, using MPSK modulation under both EGC and MRC techniques. The study conducted in [25] explored the performance of a FSO communication system utilizing single-input multiple-output (SIMO) diversity scheme in a horizontal link, under the combined effects of attenuation, pointing errors, and atmospheric turbulence. The modulation scheme selected for this study was multi-pulse pulse position modulation (MP-PPM), with atmospheric turbulence assumed to follow the Gamma-Gamma distribution, and pointing errors modeled using the Rayleigh distribution. Similarly, the performance of a SIMO FSO link with subcarrier PSK modulation scheme was investigated in [26] by combining the effects of Gamma-Gamma distributed turbulence channel, attenuation, and Beckmann-distributed pointing errors (approximated to Rayleigh distribution).

B. HAPS Based MIMO Applications

Numerous studies in the literature have extensively investigated the application of FSO communication in the context of unmanned aerial vehicle (UAV) networks. These works have specifically examined and analyzed performance metrics for various scenarios, including UAV-UAV, UAV to ground station, and ground station to UAV links [27], [28], [29], [30]. For instance, outage probability formulas have been developed for ground-to-UAV, UAV-to-UAV, and UAV-to-ground single-input single-output (SISO) FSO links, considering both Gamma-Gamma and log-normal atmospheric turbulence models, as well as the effects of position and angle-of-arrival fluctuations in [29]. The impact of environmental and FSO communication system's parameters and their optimization need to be investigated accurately to address challenges effectively and ensure maximized link availability. Recent studies have demonstrated the advantageous impact of spatial diversity techniques on enhancing the performance of FSO links, particularly in the context of HAPS-assisted FSO communication systems [31], [32], [33].

In [31], the BER performance of HAPS-assisted FSO communication system was investigated considering the impact of both attenuation and atmospheric turbulence. Notably, the effect of pointing error was not incorporated in this particular study. To overcome the challenges associated with implementing MIMO on HAPS, multiple-input single-output (MISO) technique was adopted for the uplink, while SIMO was employed for the downlink. Atmospheric turbulence was modeled using the Gamma-Gamma distribution. By implementing the M-ary pulse position modulation (MPPM) scheme, the study demonstrated a notable enhancement in the performance of HAPS-assisted FSO links through the application of both MISO and SIMO techniques. In [32], the outage probability of multi-user FSO/RF and UAV enabled communication system was examined by combining the effects of atmospheric turbulence, path loss, geometric and misalignment losses. The study particularly considers atmospheric turbulence under weak conditions, modeling turbulence-induced fading channels with a Log-normal distribution. Gaussian distribution is used to characterize the misalignment variation. Notably, for the FSO link configuration, multiple transmit apertures were employed, revealing a significant decrease in outage probability with an increasing number of transmit apertures. A bi-directional vertical ground-to-UAV MIMO FSO link was examined in [33]. In this study, atmospheric turbulence was characterized by the Log-normal distribution and authors mainly focused on deriving a statistical model for misalignment errors when multiple transceivers are used. The findings highlighted that the implementation of the MIMO scheme resulted in improved outage probability and enhanced power efficiency for the FSO communication link.

C. Contribution

Driven by the imperative to address the performance degradation induced by atmospheric turbulence, this study focuses on implementing MIMO configurations in HAPS-assisted FSO communication links. Using multiple transmitters and receivers between the source and the destination with a wide range of parameters, the main contributions of this work can be succinctly summarized as follows:

- For the first time, to the best of the authors' knowledge, our study incorporates the joint impact of AOA fluctuations, atmospheric turbulence, pointing errors, and attenuation in MIMO FSO links;
- We use the Gamma-Gamma distribution, which is widely acknowledged as the most suitable model for describing atmospheric turbulence in moderate to strong turbulence regimes. Furthermore, the Gamma-Gamma model is attractive from a performance analysis standpoint, particularly for MIMO FSO systems, where the distribution of the sum of independent Gamma-Gamma variates needs to be determined;
- The pointing error is characterized using the Hoyt distribution, a model that allows for distinct deviations in both horizontal and vertical directions;
- The AOA fluctuations are modeled using the Rayleigh distribution and we account for the impact of FoV variation in our analysis;
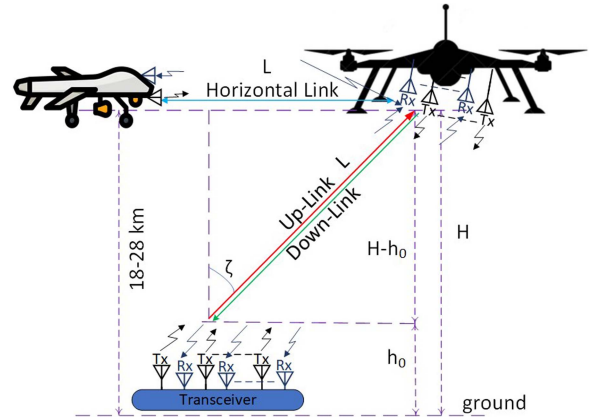

Fig. 1. MIMO FSO communication system model including uplink, downlink, and horizontal link.

- We thoroughly examine all possible link configurations, including horizontal links, downlinks, and uplinks;
- Analytical expressions for the PDF and the cumulative distribution function (CDF) of the signal-to-noise ratio (SNR) are obtained in terms of the Meijer's G function;
- Subsequently, we derive expressions for the outage probability, the average BER for OOK modulation scheme, and the ergodic capacity of an FSO link utilizing MIMO scheme and EGC technique. All these expressions are presented in terms of Meijer's G function.
- We further provide highly accurate asymptotic expressions for the outage probability and the average BER for OOK modulation scheme at high signal-to-noise ratio (SNR). These expressions are elegantly formulated in terms of simple elementary functions, offering valuable insights into the underlying physical aspects of the system.
- To validate the accuracy of the newly proposed results, we conduct numerical and computer-based Monte Carlo simulations. Notably, a perfect agreement is observed between the analytical expressions and the simulation outcomes.

D. Paper Structure

The remainder of this paper is organized as follows. Section II introduces the system and channel models. The statistical analysis of the end-to-end SNR is carried out in Section III. Analytical expressions for performance metrics, along with asymptotic results in the high SNR regime, are presented in Section IV. Section V delivers numerical and simulation results, followed by some concluding remarks in Section VI.

II. SYSTEM AND CHANNEL MODELS

The proposed system model is depicted in Fig. 1, where we consider multiple transmitters and receivers at both ground station and HAPS sides, depending on the link configurations. In this context, uplink, horizontal link, and downlink correspond to the communication channels between ground station-to-HAPS, HAPS-to-HAPS, and HAPS-to-ground station, respectively. In each link configuration, the source employs $\mathcal{M}$ transmitter apertures, while the destination utilizes $\mathcal{N}$ receiver apertures. EGC is employed as the diversity technique. The link distance
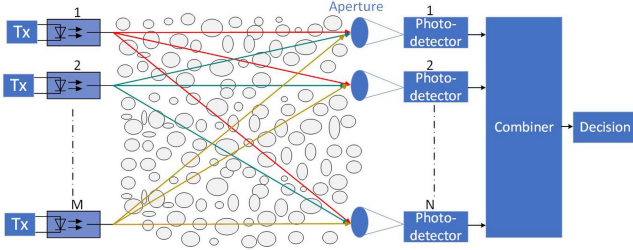
Fig. 2. MIMO structure for FSO communication link with $\mathcal{M}$ transmitters and $\mathcal{N}$ receiver apertures in atmospheric turbulence.

is represented by L, with H denoting the altitude of the HAPS. Additionally, h_0 represents the height of the ground station, and ζ is the zenith angle.

The fading channel resulting from atmospheric turbulence is characterized by the Gamma-Gamma distribution, due to its ability to provide more accurate results, especially in conditions of moderate to strong turbulence. The effect of atmospheric turbulence eddies on the propagation of optical beams from each transmitter to each photo-detector in the MIMO FSO link is illustrated in Fig. 2.

The attenuation, arising from both absorption and scattering phenomena, is determined through the application of the Beer-Lambert law, depending on the visibility parameter. We utilize a generalized pointing error model, where misalignments are characterized by a Hoyt distribution. This approach eliminates the assumption of identical jitter variance along both the vertical and horizontal axes. The effect of angle-of-arrival (AOA) fluctuations coupled with the FoV variation is also taken into account by using Rayleigh distribution. The channel statistics are derived considering the impact of MIMO application. Subsequently, the performance enhancements resulting from the implementation of MIMO scheme are demonstrated by computing the outage probability, the average BER, and the ergodic capacity for FSO downlink, horizontal link, and uplink configurations.

A. Atmospheric Turbulence

For a fading channel described by the Gamma-Gamma distribution, the probability density function (PDF) of channel is expressed as [34]

$$f_{h_{at}} = \frac{2(\alpha\beta)^{\frac{(\alpha+\beta)}{2}}}{\Gamma(\alpha)\Gamma(\beta)} h_{at}^{\frac{(\alpha+\beta)}{2}-1} K_{\alpha-\beta}\left(2\sqrt{\alpha\beta h_{at}}\right), \quad (1)$$

where $h_{at} > 0$, $\alpha = \frac{1}{\exp(\sigma_{lnX}^2)-1}$ and $\beta = \frac{1}{\exp(\sigma_{lnY}^2)-1}$, $K_a(.)$ represents the modified Bessel function of the second kind and a is its order. The log variances showing the effect of large- and small turbulent scales, denoted by σ_{lnX}^2 and σ_{lnY}^2, are obtained as [34]

$$\sigma_{lnX}^2 = \frac{0.49\left(\frac{\Omega_G-\Lambda_1}{\Omega_G+\Lambda_1}\right)^2\sigma_B^2}{\left[1+\frac{0.4(2-\overline{\Theta}_1)(\sigma_B/\sigma_R)^{12/7}}{(\Omega_G+\Lambda_1)\left(\frac{1}{3}-\frac{1}{2}\overline{\Theta}_1+\frac{1}{5}\overline{\Theta}_1^2\right)^{6/7}}+\frac{0.56(1+\Theta_1)}{\sigma_B^{-12/5}}\right]^{7/6}}, \quad (2)$$

$$\sigma_{lnY}^2 = \frac{0.51\sigma_B^2\left(1+0.69\sigma_B^{12/5}\right)^{-5/6}}{1+\left[1.20\left(\sigma_R/\sigma_B\right)^{12/5}+0.83\sigma_R^{12/5}\right]/(\Omega_G+\Lambda_1)}, \quad (3)$$

where σ_R^2 and σ_B^2 represent the Rytov variances for the unbounded plane wave and Gaussian beam, $\Omega_G = 2L/kW_G^2$ is the spot radius of the collecting lens, L stands for the link length, W_G is the Gaussian lens radius and $D_G^2 = 8W_G^2$, D_G is the receiver aperture diameter, $\Lambda_1 = \Lambda_0/(\Theta_0^2+\Lambda_0^2)$ is the Gaussian beam's Fresnel ratio at the receiver, $\Lambda_0 = 2L/kW_0^2$, W_0 is the beam radius, $\Theta_0 = 1 - L/F_0$ is the parameter of beam curvature at the transmitter, F_0 is the curvature's phase front radius, $\overline{\Theta}_1 = 1 - \Theta_1$ is the complementary parameter, and $\Theta_1 = \Theta_0/(\Theta_0^2+\Lambda_0^2)$ is the beam curvature parameter at receiver. For Gaussian beam, the Rytov variance in (2) and (3) can be calculated for a slant path link by [34]

$$\sigma_B^2 = 8.70\,k^{7/6}(H-h_0)^{5/6}\sec^{11/6}(\zeta)\text{Re}\left(\int_{h_0}^{H} C_n^2(l)\right.$$

$$\left.\times\left\{\left[\Lambda_1\xi^2+i\xi\left(1-\overline{\Theta}_1\xi\right)\right]^{5/6}-\Lambda_1^{5/6}\xi^{5/3}\right\}dl\right), \quad (4)$$

where k is the wavenumber and is equal to $k = 2\pi/\lambda$, λ indicates the beam wavelength, ζ specifies the zenith angle, h_0 is the ground station's height, H is the HAPS altitude, l is the height parameter, ξ is defined as normalized distance parameter, $C_n^2(l)$ shows the turbulence structure constant and it is given by the Hufnagel-Valley (HV) model as [34]

$$C_n^2(l) = 0.00594\left(\frac{\omega}{27}\right)^2(10^{-5}l)^{10}e^{-l/1000}$$

$$+ 2.7\times10^{-16}e^{-l/1500}+C_n^2(0)e^{-l/100}, \quad (5)$$

where ω represents the wind speed (in m/s) in terms of root mean square (rms) value and $C_n^2(0)$ denotes the turbulence structure constant's nominal value at ground level.

It should be noted that the Rytov variances for Gaussian beam can be found from (4) for downlink $\sigma_{B_d}^2$ and uplink $\sigma_{B_u}^2$ by utilizing the normalized distance parameter $\xi = \frac{(l-h_0)}{(H-h_0)}$ for downlink propagation and $\xi = 1 - \frac{(l-h_0)}{(H-h_0)}$ for uplink propagation, respectively. Rytov variances for plane wave ($\sigma_{R_d}^2$, $\sigma_{R_u}^2$) can also be obtained from (4) by setting the parameters $\Theta_1 = 1$ and $\Lambda_1 = 0$ together with the related normalized distance parameter ξ.

When the communication link is horizontal, the Rytov variances of the Gaussian beam σ_B^2 and plane wave σ_R^2 can be expressed as [34]

$$\sigma_{B_h}^2 = 4.75\,C_n^2(H)k^{\frac{7}{6}}L^{\frac{11}{6}}\left\{0.40\left[(1+2\Theta_1)^2+4\Lambda_1^2\right]^{\frac{5}{12}}\right.$$

$$\left.\times\cos\left[\frac{5}{6}\tan^{-1}\left(\frac{1+2\Theta_1}{2\Lambda_1}\right)\right]-\frac{11}{16}\Lambda_1^{5/6}\right\}, \quad (6)$$

$$\sigma_{R_h}^2 = 1.23\,C_n^2(H)k^{\frac{7}{6}}L^{\frac{11}{6}}. \quad (7)$$

B. Atmospheric Attenuation

In addition to atmospheric turbulence, the impact of absorption and scattering on the propagating optical beam is significant. The attenuation caused by these phenomena is accurately modeled using the Beer-Lambert law, defined as

$$h_{al} = \exp(-C(\lambda)\,L), \tag{8}$$

where $C(\lambda)$ represents the attenuation coefficient. As reported in [35], the attenuation coefficient is determined based on the visibility parameter V (in km) and the wavelength λ (in nm) as

$$C(\lambda) = \frac{3.912\,(\lambda/550)^{-q}}{V}, \tag{9}$$

where

$$q = \begin{cases} 0, & \text{for } V < 0.5\,\text{Km} \\ 0.16V + 0.34, & \text{for } 1\,\text{Km} < V < 6\,\text{Km} \\ 1.3, & \text{for } 6\,\text{Km} < V < 50\,\text{Km} \\ 1.6, & \text{for } V > 50\,\text{Km} \end{cases}. \tag{10}$$

C. Angle of Arrival Fluctuations

According to [5], the effect of sidelobs can be neglected, and therefore the channel state for the AOA fluctuations can be modeled as

$$h_{af} = \begin{cases} 1, & \theta_d \le \theta_{FOV} \\ 0, & \theta_d > \theta_{FOV} \end{cases}, \tag{11}$$

where θ_d and θ_{FOV} refer the deviation and FoV angles, respectively. Utilizing the Rayleigh distribution, the PDF of the random variable θ_d can be expressed as [5]

$$f_{\theta_d}(\theta_d) = \frac{\theta_d}{\sigma_0^2} \exp\left(-\frac{\theta_d^2}{2\sigma_0^2}\right), \tag{12}$$

where $\theta_d \ge 0$ and σ_0^2 represents the variance of θ_d.

D. Pointing Error

In this work, we consider a generalized pointing error model based on the Hoyt distribution, where a different jitter in horizontal s and vertical z beam displacements is considered. In this realistic setup, the PDF of the misalignment using polar coordinates can be expressed as [36, Eq.(3)]

$$f_{r,\varphi}(r,\varphi) = \frac{r}{2\pi q_H \sigma_s^2} \exp\left(-\frac{r^2 \xi(\varphi)}{2 q_H^2 \sigma_s^2}\right), \tag{13}$$

where

$$\xi(\varphi) = q_H^{-2}\left[1 - (1 - q_H^2)\cos^2\varphi\right], \tag{14}$$

with $q_H = \sigma_z/\sigma_s \in (0,1]$ refers to the ratio of horizontal and vertical beam displacements, σ_s^2 and σ_z^2 are the beam jitters variances, $s = r\cos(\varphi)$, and $z = r\sin(\varphi)$. Marginalizing (13) with respect to φ, the radial displacement at the receiver detector r is characterized by a Hoyt distribution with the PDF given

by [36, Eq.(5)] as

$$f_r(r) = \frac{r}{q_H \sigma_s^2} \exp\left(-\frac{(1+q_H^2)\,r^2}{4\,q_H^2 \sigma_s^2}\right) I_0\left(\frac{(1-q_H^2)\,r^2}{4\,q_H^2 \sigma_s^2}\right), \tag{15}$$

where I_0 represents the vth-order modified Bessel function of the first kind. As outlined in [37], the pointing loss conditioned on θ_d is a function of the radial displacement r defined as

$$h_{pl|\theta_d} = A_0\,e^{-\frac{2r^2}{w_e^2}}\cos\theta_d. \tag{16}$$

By using [36, Eq.(11)] with some manipulations, the PDF of h_{pl} conditioned on θ_d can be given in its integral form as

$$f_{h_{pl}|\theta_d}(h_{pl}) = \frac{\eta_s^2}{2\pi q_H} \int_{-\pi}^{\pi} \frac{h_{pl}^{\eta_s^2 \xi(\varphi)-1}}{(A_0 \cos\theta_d)^{\eta_s^2 \xi(\varphi)}}\,d\varphi, \tag{17}$$

where $\omega_e = \sqrt{\omega_b^2 \sqrt{\pi}\,\text{erf}(v)/(2ve^{-v^2})}$ stands for the equivalent beam waist, ω_b is beam waist, $\text{erf}(.)$ is error function, $\eta_s = \frac{\omega_e}{2\sigma_s}$, $v = \sqrt{\frac{\pi r_a^2}{2\omega_b^2}}$, r_a is receiver aperture radius, $A_0 = (\text{erf}(v))^2$ is the fraction of the collected power at $r = 0$, and $0 \le h_{pl} \le A_0 \cos\theta_d$.

Note that the finite-limit integral in (17) can be readily computed using suitable numerical methods that can be found in existing literature. Furthermore, when both displacements have common jitter variance (i.e. $\sigma_s^2 = \sigma_z^2 = \sigma^2$), the radial displacement at the receiver r is determined by a Rayleigh distribution, and (17) simplifies to [38, Eq.(2)] by setting $q_H = 1$ as

$$f_{h_{pl}|\theta_d}(h_{pl}) = \frac{\eta^2}{(A_0 \cos\theta_d)^{\eta^2}} h_{pl}^{\eta^2-1}, \tag{18}$$

where $\eta = \omega_e/(2\sigma)$.

E. Channel Model

Assuming a MIMO FSO system with $\mathcal{M}$ transmitters and $\mathcal{N}$ receiver apertures, resulting in an $\mathcal{M} \times \mathcal{N}$ channel matrix, and employing the EGC spatial diversity technique, the photocurrent of the nth photodetector corresponding to the mth transmitter at the output of combiner can be written as

$$y_{mn}(t) = \frac{\eta}{\mathcal{MN}} x_{mn}(t) \sum_{m=1}^{\mathcal{M}} \sum_{n=1}^{\mathcal{N}} h_{mn} + \sum_{n=1}^{\mathcal{N}} n_n(t), \tag{19}$$

where η is the responsivity of the photodetector, $x_{mn}(t)$ denotes the transmitted signal sent by the mth transmitter, h_{mn} represents the irradiance received by the nth receiver aperture corresponding to the mth transmitter, and $n_n(t) \sim (0, N_0/2)$ is the AWGN at the nth photodetector. Using the relationships $h = \sum_{m=1}^{\mathcal{M}} \sum_{n=1}^{\mathcal{N}} h_{mn}$ and $Z_{mn} = \sum_{n=1}^{\mathcal{N}} n_n(t)$, (19) becomes

$$y_{mn}(t) = \frac{\eta}{\mathcal{MN}} x_{mn}(t)h + Z_{mn}. \tag{20}$$

The instantaneous SNR can be formulated as

$$\gamma = \frac{(\eta h)^2}{(\mathcal{MN})^2 N_0}. \tag{21}$$

As demonstrated in [39], [40], the sum of Gamma-Gamma random variables can be effectively approximated by another Gamma-Gamma distributed random variable. Subsequently, the resulting PDF of h_{at} is determined based on the new shaping parameters α_1 and β_1 as follows

$$f_{h_{at}} = \frac{2 \left(\frac{\alpha_1 \beta_1}{\mathcal{MN}} \right)^{\frac{\alpha_1 + \beta_1}{2}}}{\Gamma(\alpha_1)\Gamma(\beta_1)} h_{at}^{\frac{\alpha_1 + \beta_1}{2} - 1} K_{\alpha_1 - \beta_1} \left(2\sqrt{\frac{\alpha_1 \beta_1}{\mathcal{MN}} h_{at}} \right),$$

$$(22)$$

where $\alpha_1 = \mathcal{MN}\alpha$ and $\beta_1 = \mathcal{MN}\beta$. We consider that all turbulence-induced fading h_{mn}'s are modeled as independent and identically distributed (i.i.d.) random variables, which is justified for aperture separation distances of the order of centimeters and link distances of the order of kilometers [15]. For the atmospheric attenuation, considering that the separation distance between the lasers and the photo detectors is very large compared to the separation distance between the lasers, we can assume that we have a common atmospheric attenuation modeled by (8) in the paper. Furthermore, it is assumed that the receivers are positioned very closely together and that the beam radius is sufficiently large to allow each receiver's relative displacement with respect to the initial pointing to be considered negligible. As a result, the pointing error model in (18) can also be applied to FSO systems having more than one photodetector [21]. Hence, the combined channel state can be expressed by

$$h = h_{al}h_{at}h_{pl}h_{af}, \tag{23}$$

where the PDF of the channel state conditioned on θ_d using the relationship $h_{ag} = h_{al}h_{at}h_{pl}$ can be written as

$$f_{h_{ag}|\theta_d}(h_{ag}) = \int_\Delta^\infty \frac{1}{h_{al}h_{at}} f_{h_{pl}|\theta_d} \left(\frac{h_{ag}}{h_{al}h_{at}} \right) f_{h_{at}}(h_{at}) dh_{at},$$

$$(24)$$

with $\Delta = h_{ag}/(A_0 h_{al}\cos\theta_d)$. After thorough calculations, as elucidated in Appendix A, we derive the resulting PDF of the combined channel state as

$$f_h(h) = \frac{\eta_s^2 \left(1 - \exp\left(-\frac{\theta_{FOV}^2}{2\sigma_0^2} \right) \right)}{2\pi q_H \Gamma(\alpha_1)\Gamma(\beta_1) h}$$

$$\times \int_{-\pi}^{\pi} G_{1,3}^{3,0} \left[\frac{\alpha_1 \beta_1\, h}{\mathcal{MN}A_0 h_{al}} \left| \begin{matrix} 1 + \eta_s^2\xi(\varphi) \\ \alpha_1, \beta_1, \eta_s^2\xi(\varphi) \end{matrix} \right. \right] d\varphi$$

$$+ \delta(h) \exp\left(-\frac{\theta_{FOV}^2}{2\sigma_0^2} \right), \tag{25}$$

where $G_{\cdot,\cdot}^{\cdot,\cdot}[\cdot]$ denotes the Meijer's G function [41, Eq.(9.301)] and $\delta(\cdot)$ stands for the Dirac-delta function.

III. END-TO-END SNR STATISTICS

A. Probability Density Function

The instantaneous SNR of the MIMO FSO system, under the assumption $\mathbb{E}[h^2] = 1$ where $\mathbb{E}[\cdot]$ denotes the expected value, can be re-written as $\gamma = \overline{\gamma}h^2$, where $\overline{\gamma}$ represents the average

SNR. Additionally, assuming that the channel presents independent and identical distribution (i.i.d.) characteristics, the average SNR can be expressed as $\overline{\gamma} = \mathcal{MN}\overline{\gamma}_l$, where $\overline{\gamma}_l$ signifies the average SNR of each link between the transmitter and receiver. By using this random variable transformation, the resulting PDF of γ can be derived from (25) as

$$f_\gamma(\gamma) = \frac{\eta_s^2 \left(1 - \exp\left(-\frac{\theta_{FOV}^2}{2\sigma_0^2} \right) \right)}{4\pi q_H \Gamma(\alpha_1)\Gamma(\beta_1)\, \gamma}$$

$$\times \int_{-\pi}^{\pi} G_{1,3}^{3,0} \left[\frac{\alpha_1 \beta_1}{\mathcal{MN}A_0 h_{al}} \sqrt{\frac{\gamma}{\overline{\gamma}}} \left| \begin{matrix} 1 + \eta_s^2\xi(\varphi) \\ \alpha_1, \beta_1, \eta_s^2\xi(\varphi) \end{matrix} \right. \right] d\varphi$$

$$+ \exp\left(-\frac{\theta_{FOV}^2}{2\sigma_0^2} \right) \frac{1}{2\sqrt{\overline{\gamma}\gamma}} \delta\left(\sqrt{\frac{\gamma}{\overline{\gamma}}} \right). \tag{26}$$

B. Cumulative Distribution Function

The CDF of the overall SNR γ for a MIMO system, accounting for pointing errors and AOA fluctuations, can be obtained by employing

$$F_\gamma(\gamma) = \int_0^\gamma f_\gamma(x) dx. \tag{27}$$

Following the derivations provided in Appendix B, the analytical expression of the SNR CDF can be derived as

$$F_\gamma(\gamma) = \frac{\eta_s^2 \left(1 - \exp\left(-\frac{\theta_{FOV}^2}{2\sigma_0^2} \right) \right)}{2\pi q_H \Gamma(\alpha_1)\Gamma(\beta_1)}$$

$$\times \int_{-\pi}^{\pi} G_{2,4}^{3,1} \left[\frac{\alpha_1 \beta_1}{\mathcal{MN}A_0 h_{al}} \sqrt{\frac{\gamma}{\overline{\gamma}}} \left| \begin{matrix} 1, 1 + \eta_s^2\xi(\varphi) \\ \alpha_1, \beta_1, \eta_s^2\xi(\varphi), 0 \end{matrix} \right. \right] d\varphi$$

$$+ \exp\left(-\frac{\theta_{FOV}^2}{2\sigma_0^2} \right) H\left(\sqrt{\frac{\gamma}{\overline{\gamma}}} \right), \tag{28}$$

where $H(\cdot)$ representss the Heaviside step function.

IV. END-TO-END PERFORMANCE METRICS

A. Outage Probability

1) Exact Analysis: The probability that the instantaneous SNR is below a predefined threshold, γ_{th}, referred to as the outage probability, can be expressed as

$$P_{out} = P_r(\gamma \leq \gamma_{th}) = F_\gamma(\gamma_{th}). \tag{29}$$

By substituting (28) into (29), the resulting outage probability for a MIMO FSO link is determined as

$$P_{out} = \frac{\eta_s^2 \left(1 - \exp\left(-\frac{\theta_{FOV}^2}{2\sigma_0^2} \right) \right)}{2\pi q_H \Gamma(\alpha_1)\Gamma(\beta_1)}$$

$$\times \int_{-\pi}^{\pi} G_{2,4}^{3,1} \left[\frac{\alpha_1 \beta_1}{\mathcal{MN}A_0 h_{al}} \sqrt{\frac{\gamma_{th}}{\overline{\gamma}}} \left| \begin{matrix} 1, 1 + \eta_s^2\xi(\varphi) \\ \alpha_1, \beta_1, \eta_s^2\xi(\varphi), 0 \end{matrix} \right. \right] d\varphi$$

$$+ \exp\left(-\frac{\theta_{FOV}^2}{2\sigma_0^2} \right). \tag{30}$$

It is important to note that, despite the presence of a φ-dependent integration in the derived outage probability result in (30), this expression can be easily and efficiently evaluated using software packages like Matlab or Mathematica. Furthermore, in the specific case where $q_H = 1$, we obtain the outage probability in exact closed-form as

$$
P_{\text{out}} = \frac{\eta_s^2 \left(1 - \exp\left(-\frac{\theta_{FOV}^2}{2\sigma_0^2}\right)\right)}{\Gamma(\alpha_1)\Gamma(\beta_1)}
$$

$$
\times \, G_{2,4}^{3,1}\left[\frac{\alpha_1\beta_1}{\mathcal{MN}A_0 h_{al}} \sqrt{\frac{\gamma_{\text{th}}}{\overline{\gamma}}} \,\middle|\, \begin{matrix} 1, 1 + \eta_s^2 \\ \alpha_1, \beta_1, \eta_s^2, 0 \end{matrix}\right] + \exp\left(-\frac{\theta_{FOV}^2}{2\sigma_0^2}\right).
$$
(31)

2) Asymptotic Analysis: A highly accurate asymptotic result for the outage probability expression in (30) can be achieved in the high SNR regime by using [42, Eq.(1.8.5)] with some algebraic manipulations as

$$
P_{\text{out}} \underset{\overline{\gamma}\gg 1}{\approx} \frac{\eta_s^2 \left(1 - \exp\left(-\frac{\theta_{FOV}^2}{2\sigma_0^2}\right)\right)}{2\pi q_H \Gamma(\alpha_1)\Gamma(\beta_1)} \int_{-\pi}^{\pi} \sum_{i=1}^{3} \mathcal{U}_i \left(\frac{\gamma_{\text{th}}}{\overline{\gamma}}\right)^{\theta_i} d\varphi
$$

$$
+ \exp\left(-\frac{\theta_{FOV}^2}{2\sigma_0^2}\right).
$$
(32)

where $\theta_i = \{\frac{\alpha_1}{2}, \frac{\beta_1}{2}, \frac{\eta_s^2\xi(\varphi)}{2}\}$,

$$
\mathcal{U}_1 = \frac{\Gamma(\beta_1 - \alpha_1)}{\alpha_1 \left(\eta_s^2\xi(\varphi) - \alpha_1\right)} \left(\frac{\alpha_1\beta_1}{\mathcal{MN}A_0 h_{al}}\right)^{\alpha_1},
$$
(33)

$$
\mathcal{U}_2 = \frac{\Gamma(\alpha_1 - \beta_1)}{\beta_1 \left(\eta_s^2\xi(\varphi) - \beta_1\right)} \left(\frac{\alpha_1\beta_1}{\mathcal{MN}A_0 h_{al}}\right)^{\beta_1},
$$
(34)

$$
\mathcal{U}_3 = \frac{\Gamma(\alpha_1 - \eta_s^2\xi(\varphi))\Gamma(\beta_1 - \eta_s^2\xi(\varphi))}{\eta_s^2\xi(\varphi)} \left(\frac{\alpha_1\beta_1}{\mathcal{MN}A_0 h_{al}}\right)^{\eta_s^2\xi(\varphi)}.
$$
(35)

It is noteworthy that the outage probability expression in (32) comprises only summations of basic elementary functions, a notable simplification compared to the exact expression formulated in terms of the Meijer's G function in (30). This simplified result, which is analytically more tractable, demonstrates high accuracy and converges perfectly to the exact result at high SNR. Furthermore, we may easily obtain the diversity order of the MIMO FSO system from (32) as follows

$$
G_d = \min\left(\frac{\mathcal{MN}\alpha}{2}, \frac{\mathcal{MN}\beta}{2}, \frac{\eta_s^2\xi(\varphi)}{2}\right).
$$
(36)

B. Average Bit-Error Rate

1) Exact Analysis: The average BER of IM/DD with OOK can be expressed as $P(e) = P(0)P(e|0) + P(1)P(e|1)$, where $P(0)$ and $P(1)$ represent the probabilities of transmitting 0 and 1 bits, respectively. Additionally, $P(e|0)$ and $P(e|1)$ denote the conditional error probabilities when bits 0 and 1 are transmitted, respectively. Assuming $P(0) = P(1) = \frac{1}{2}$ and $P(e|0) = P(e|1)$, the average BER formulated as [36]

$$
\overline{P}_e = \frac{1}{2} \int_0^{\infty} \text{erfc}\left(\frac{\sqrt{\gamma}}{2}\right) f_\gamma(\gamma) \, d\gamma,
$$
(37)

can be obtained in terms of the Meijer's G function as demonstrated in Appendix C as

$$
\overline{P}_e = \frac{\eta_s^2 \left(1 - \exp\left(-\frac{\theta_{FOV}^2}{2\sigma_0^2}\right)\right) 2^{\alpha_1+\beta_1-1}}{(4\pi)^2 q_H \Gamma(\alpha_1)\Gamma(\beta_1)\Gamma(1/2)} \int_{-\pi}^{\pi} d\varphi
$$

$$
\times \, G_{3,6}^{5,2}\left[\left(\frac{\alpha_1\beta_1}{2\mathcal{MN}A_0 h_{al}\sqrt{\overline{\gamma}}}\right)^2 \middle| \begin{matrix} 1, \frac{1}{2}, 1 + \frac{\eta_s^2\xi(\varphi)}{2} \\ \frac{\alpha_1}{2}, \frac{\alpha_1+1}{2}, \frac{\beta_1}{2}, \frac{\beta_1+1}{2}, \frac{\eta_s^2\xi(\varphi)}{2}, 0 \end{matrix}\right]
$$

$$
+ \frac{1}{2} \exp\left(-\frac{\theta_{FOV}^2}{2\sigma_0^2}\right).
$$
(38)

Note that in this study, we focus on investigating the average BER for OOK modulation. OOK modulation is chosen due to its widespread use in practical IM/DD FSO systems, owing to its simplicity and robustness against laser nonlinearity.

2) Asymptotic Analysis: The average BER expression in (37) can be reformulated in terms of the CDF of γ through the application of integration by parts, yielding

$$
\overline{P}_e = \frac{1}{4\Gamma(1/2)} \int_0^{\infty} \gamma^{-\frac{1}{2}} \exp\left(-\frac{\gamma}{4}\right) F_\gamma(\gamma) \, d\gamma.
$$
(39)

In alignment with the asymptotic analysis of the outage probability, a simpler mathematical expression for the average BER for OOK modulation can be derived in the high SNR regime. This is achieved by substituting the high SNR CDF expression, obtained from (32), into (39), and employing [41, Eq.(3.381/4)] as

$$
\overline{P}_e \underset{\overline{\gamma}\gg 1}{\approx} \frac{\eta_s^2 \left(1 - \exp\left(-\frac{\theta_{FOV}^2}{2\sigma_0^2}\right)\right)}{4\pi q_H \Gamma(\alpha_1)\Gamma(\beta_1)\Gamma(1/2)}
$$

$$
\times \int_{-\pi}^{\pi} \sum_{i=1}^{3} \mathcal{U}_i \Gamma\left(\theta_i + \frac{1}{2}\right) \left(\frac{4}{\overline{\gamma}}\right)^{\theta_i} d\varphi + \frac{1}{2} \exp\left(-\frac{\theta_{FOV}^2}{2\sigma_0^2}\right).
$$
(40)

C. Ergodic Capacity

The ergodic capacity for FSO systems with IM/DD can be computed as

$$
\overline{C} \triangleq \mathbb{E}[\log_2(1 + c\,\gamma)],
$$
(41)

where c is a constant, specifically equal to $c = e/(2\pi)$ in the case of IM/DD technique [43, Eq. (26)]. By substituting (26) into (41), using the Meijer's G function representation of $\ln(1 + c\,\gamma)$ as $G_{2,2}^{1,2}\left[c\gamma \middle| \begin{matrix} 1, 1 \\ 1, 0 \end{matrix}\right]$ [44, Eq. (8.4.6/5)], along with intergration using [44, Eq. (2.24.1/1)] and applying the RV transformation $t = \sqrt{x/\overline{\gamma}}$, the ergodic capacity of the MIMO FSO system can be derived after some simplifications as

$$
\overline{C} = \frac{\eta_s^2 \left(1 - \exp\left(-\frac{\theta_{FOV}^2}{2\sigma_0^2}\right)\right) 2^{\alpha_1+\beta_1-2}}{(2\pi)^2 q_H \Gamma(\alpha_1)\Gamma(\beta_1)\ln(2)} \int_{-\pi}^{\pi} d\varphi
$$

$$
G_{3,7}^{7,1}\left[\left(\frac{\alpha_1\beta_1}{4\mathcal{MN}A_0 h_{al}\sqrt{c\overline{\gamma}}}\right)^2 \middle| \begin{matrix} 0, 1, 1 + \frac{\eta_s^2\xi(\varphi)}{2} \\ \frac{\alpha_1}{2}, \frac{\alpha_1+1}{2}, \frac{\beta_1}{2}, \frac{\beta_1+1}{2}, \frac{\eta_s^2\xi(\varphi)}{2}, 0, 0 \end{matrix}\right].
$$
(42)

TABLE I
SYSTEM PARAMETERS

Symbol	Value	Symbol	Value
λ	1550 nm	F_0	∞
ω	30 m/s	ξ	$40°$
$C_n^2(0)$	1.7×10^{-13} m$^{-2/3}$	V	10 km
h_0	10 m	H	20 km
D_G, W_0	1 cm, 1 mm	$\mathcal{M}$	2
q_H	0.8	$\mathcal{N}$	2
σ_s	$1 \times r_a$	σ_z	$q_H \times \sigma_s$
σ_0	12 mrad	θ_{FOV}	60 mrad
ω_b	$3 \times r_a$	$\overline{\gamma}_l$	30 dB
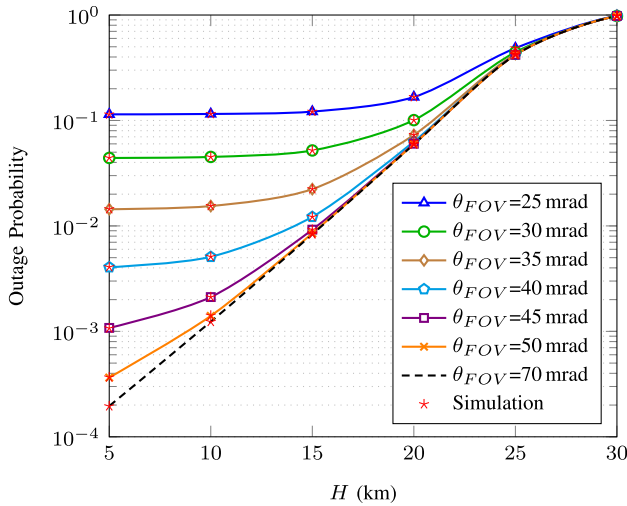
Fig. 3. Outage probability for downlink versus altitude of air platform for various FoVs.

Fig. 4. Downlink outage probability versus average SNR for various beam deviations.

V. RESULTS AND DISCUSSION

In this section, we illustrate the mathematical formalism outlined above by employing the set of parameters listed in Table I, which are mostly based on the standard settings for system parameters [45] and references therein. Any parameters not explicitly mentioned in Table I are explicitly stated in the figures. Monte-Carlo simulations are also included and compared with the obtained analytical results over 10^7 realizations. A very good match is observed between the derived analytical expressions and the corresponding simulated outcomes, thereby confirming the accuracy of the proposed results.

The outage performance of MIMO FSO downlink channel is illustrated as function of the altitude of HAPS for different values of the receiver FoV in Fig. 3. It can be deduced from Fig. 3 that the smaller the value of FoV (e.g., $\theta_{FOV} = 25$ mrad), the higher will be the outage probability of the system. Moreover, it can be clearly seen from this figure that increasing the altitude of HAPS causes slight increase in the outage probability for small values of FoV. However, the effect of higher altitude of HAPS becomes more dominant on the outage probability performance when FoV is sufficiently large (e.g., $\theta_{FOV} = 70$ mrad). This can be interpreted 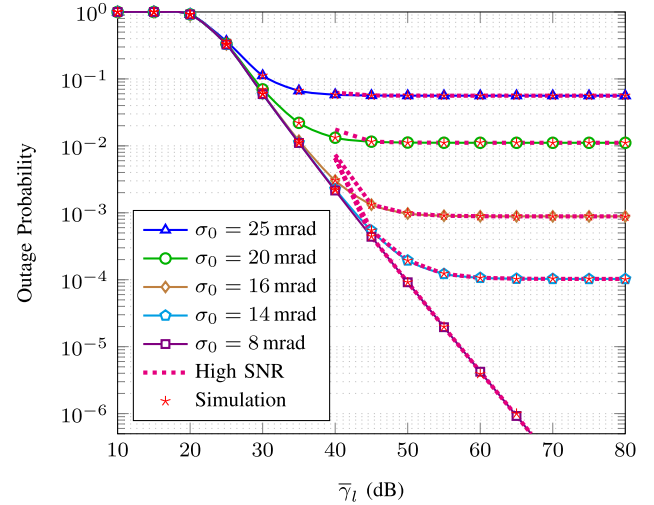as the outage probability is almost saturated at the higher levels when FoV is below a certain narrowness and the effect of other parameters will be limited but if the FoV is sufficiently large then the impact of the altitude becomes remarkable.

In Fig. 4, the outage performance variation with the average SNR of each link for various values of random orientation deviations due to AOA fluctuations is presented for a MIMO FSO downlink. It can be observed from Fig. 4 that an increase in the AOA fluctuations degrades the performance of HAPS-assisted MIMO FSO link significantly. For a fixed average SNR at $\overline{\gamma}_l = 45$ dB, the outage probability increases from $P_{\text{out}} \sim 5.45 \times 10^{-4}$ to $P_{\text{out}} \sim 5.65 \times 10^{-2}$ with the increase of the orientation deviation from $\sigma_0 = 14$ mrad to $\sigma_0 = 25$ mrad. It can also be seen from Fig. 4 that the performance of MIMO FSO communication system enhances when the average SNR increases. However, the decrease trend in the outage probability stops after a certain value of average SNR and the outage probability does not change even if the average SNR proceeds to increase. For example, when the orientation deviation due to AOA fluctuations is $\sigma_0 = 16$ mrad, the outage probability decreases from $P_{\text{out}} \sim 3.27 \times 10^{-1}$ to $P_{\text{out}} \sim 1.32 \times 10^{-3}$ when average SNR is increased from $\overline{\gamma}_l = 25$ dB to $\overline{\gamma}_l = 45$ dB then, the outage probability keeps almost the same value and does not decrease with the increasing average SNR. The decrease in the outage probability with the rise of average SNR up to a certain point can also be noted from all the following average SNR dependent plots. For instance, the outage probability when $\sigma_0 = 16$ decreases by two orders of magnitude for a change in the average SNR from $\overline{\gamma}_l = 10$ dB to $\overline{\gamma}_l = 35$ dB. The reason for this big change is that the received signal power becomes much higher than the channel impairments and noise artifacts at higher SNR level. The asymptotic results of the outage probability at high average SNR values obtained by using (32) are also included in Fig. 4. Obviously, the asymptotic results of the outage probability match perfectly the analytical results in the high SNR regime. This justifies the accuracy and the tightness of the derived asymptotic expression in (32).
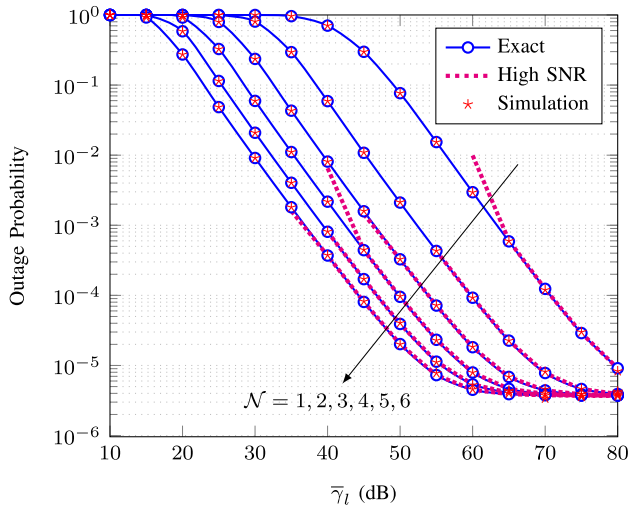
Fig. 5. Downlink outage probability versus average SNR for various values of receiver aperture number with $\mathcal{M} = 1$.

Fig. 7. Outage probability of downlink against the average SNR for various values of zenith angle.
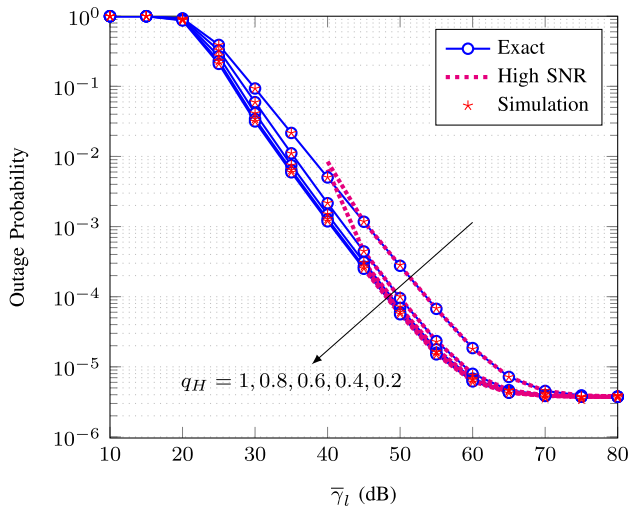

Fig. 6. Outage probability of downlink versus average SNR for different ratios of horizontal and vertical beam deviations.

In Fig. 5, we applied SIMO spatial diversity technique to HAPS-to-ground FSO downlink and observed the outage performance. As expected, a significant increase in the performance is achieved by increasing the number of receiver apertures, which demonstrates the usefulness of the spatial diversity technique. For a single transmitter $\mathcal{M} = 1$ and fixed average SNR $\overline{\gamma}_l = 40$ dB, single receiver aperture $\mathcal{N} = 1$ yields an outage probability of $P_{\text{out}} \sim 7.05 \times 10^{-1}$ however, outage probability drops to $P_{\text{out}} \sim 3.75 \times 10^{-4}$ when the number of receiver apertures is increased to $\mathcal{N} = 6$. This considerable performance improvement proves that the spatial diversity technique remains as a remarkable tool concerning the mitigation of the fading effect for an FSO link. Other outcomes, specifically for the high SNR asymptotic results, can be clearly seen similar to Fig. 4 above. The outage probability under different q_H values is depicted in Fig. 6. It can be concluded from Fig. 6 that the performance of MIMO FSO communication system improves when the beam orientation deviation presents an asymmetrical
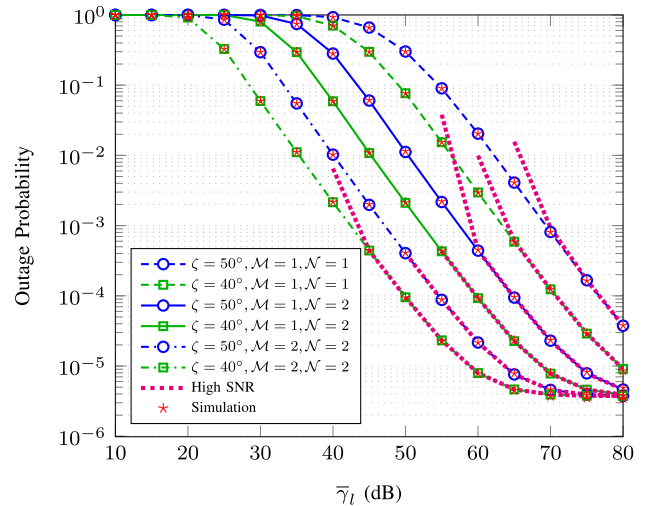
behavior. For an average SNR $\overline{\gamma}_l = 35$ dB, the outage probability takes the value of $P_{\text{out}} \sim 2.16 \times 10^{-2}$ when horizontal and vertical orientation deviations are equal to each other ($q_H = 1$) however, the outage probability falls to $P_{out} \sim 5.93 \times 10^{-3}$ when the ratio of horizontal and vertical beam deviations becomes $q_H = 0.2$. Another conclusion to be drawn from Fig. 6 is that the outage probability values approach each other when q_H decreases. This can be seen on setting $\overline{\gamma}_l = 35$ dB in Fig. 6, when the outage probability takes values of $P_{\text{out}} \sim 5.93 \times 10^{-3}$ and $P_{\text{out}} \sim 6.41 \times 10^{-3}$ for slightly different values of q_H as $q_H = 0.2$ and $q_H = 0.4$, respectively.

The impact of the zenith angle ζ as well as the number of transmitter and receiver apertures $\mathcal{M}$ and $\mathcal{N}$ on the outage performance of MIMO FSO downlink is reflected in Fig. 7. The noticeable mitigation effect of MIMO scheme is obviously seen from Fig. 7. For $\overline{\gamma}_l = 45$ dB and $\zeta = 50°$, the outage probability decreases from $P_{\text{out}} \sim 6.62 \times 10^{-1}$ to $P_{\text{out}} \sim 1.97 \times 10^{-3}$ with a change of the number of transmitter and receiver apertures from $\mathcal{M} = 1, \mathcal{N} = 1$ to $\mathcal{M} = 2, \mathcal{N} = 2$. This significant performance improvement demonstrates the undeniable benefit of MIMO application for FSO links. The effect of zenith angle is also seen from Fig. 7. It can be shown that keeping the zenith angle as small as possible results in a better performance of HAPS-assisted MIMO FSO communication systems. For a $\mathcal{M} = 1, \mathcal{N} = 2$ SIMO scheme and $\overline{\gamma}_l = 40$ dB average SNR value, the outage probability moves downward from $P_{\text{out}} \sim 2.82 \times 10^{-1}$ to $P_{\text{out}} \sim 5.89 \times 10^{-2}$ with the decrease of zenith angle from $\zeta = 50°$ to $\zeta = 40°$.

To further illustrate the effect of the receiver FoV on the performance of MIMO FSO uplink, the average BER for OOK and the outage probability are presented in both Figs. 8 and 9. It can be seen from both figures that the greater the value of the receiver FoV, the better will be the performance of FSO ground-to-HAPS links. Moreover, we can observe from Fig. 9 that increasing the average SNR $\overline{\gamma}_l$ improves the average BER performance to a limited extent when FoV is quite small, e.g., the average BER does not change after $\overline{\gamma}_l \sim 40$ dB when $\theta_{FOV} = 25$ mrad. This indicates that the receiver FoV of FSO communication systems
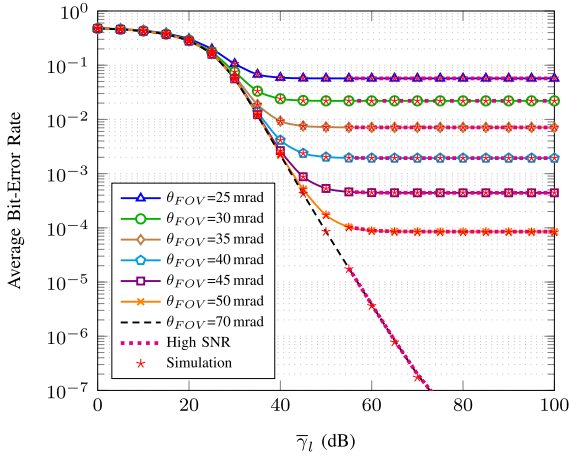
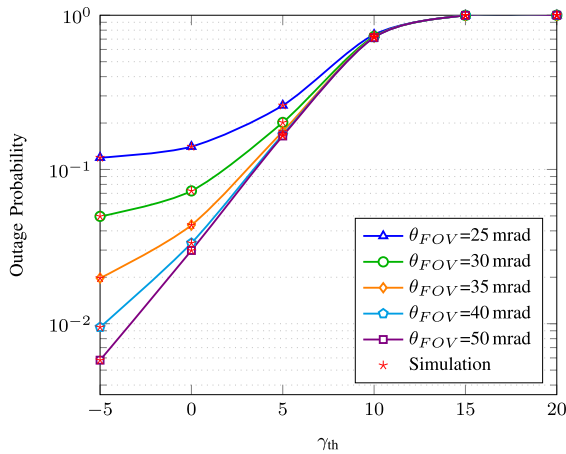Fig. 8. Average BER for OOK of uplink against the average SNR for various values of FoV.

Fig. 10. Average BER of uplink against the average SNR for SISO, SIMO, MISO, and MIMO configurations.

Fig. 9. Outage probability of uplink versus threshold SNR for different values of FoV.

Fig. 11. Average BER of uplink against the average SNR for various values of receiver aperture diameter, transmitter, and receiver aperture number.

should be kept larger however, an optimization is required since the background noise effect will also be increased with larger FoV values. In addition, Fig. 9 shows that the outage probability is prone to increase monotonically with the increase of threshold SNR γ_{th}. This increase remains slight for smaller values of FoV due to almost saturated outage probability level while the increase of outage probability is faster for large values of FoV. Furthermore, it can be observed from Fig. 8 that in the high SNR regime, the asymptotic expression of the average BER derived in (40) converges perfectly to the exact result proving the tightness of this asymptotic result.

In Fig. 10, the average BER performance of FSO uplink is investigated for SISO, SIMO, MISO, and MIMO configurations. One of the most important outcomes of this figure is the diversity gain achieved by increasing the number of transmit $\mathcal{M}$ and receive $\mathcal{N}$ apertures. This result aligns perfectly with the diversity order expression given in (36) which is a function of $\mathcal{M}\mathcal{N}$. For instance, for $\overline{\gamma}_l = 40$ dB, changing the spatial diversity configuration from $\mathcal{M} = 1, \mathcal{N} = 1$ (SISO) to $\mathcal{M} = 1, \mathcal{N} = 2$ (SIMO) and $\mathcal{M} = 2, \mathcal{N} = 2$ (MIMO) reduces the average BER from $\overline{P}_e \sim 2.44 \times 10^{-1}$ to $\overline{P}_e \sim 4.98 \times 10^{-2}$
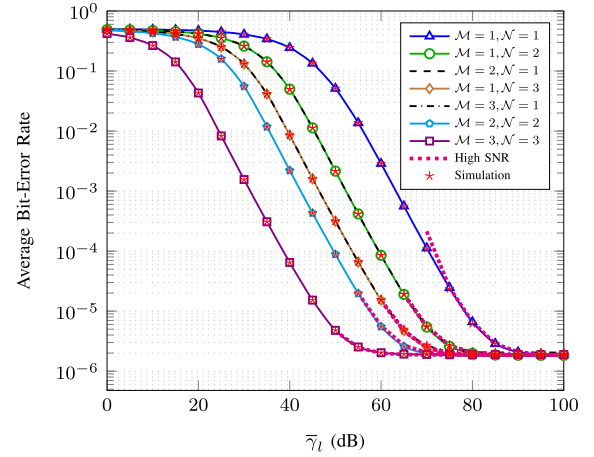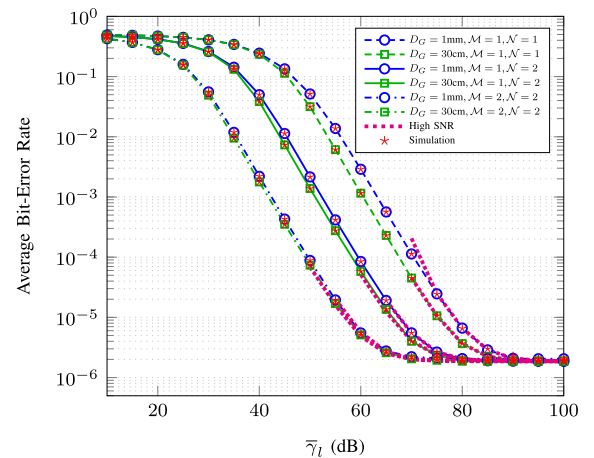
and $\overline{P}_e \sim 2.2 \times 10^{-3}$ which indicates that MIMO presents the best performance among the presented diversity schemes. Note that in this evaluation, SIMO and MISO present the same BER performance because the diversity gain is proportional to $\mathcal{M}\mathcal{N}$. It is also observed from Fig. 10 that the required SNR level for MIMO with more link numbers is smaller than that of with less link numbers. For example, to achieve a BER value of $\overline{P}_e \sim 10^{-3}$, the required SNR levels are approximately as $\overline{\gamma}_l = 30$ dB, $\overline{\gamma}_l = 40$ dB, and $\overline{\gamma}_l = 60$ dB for $\mathcal{M} = 3, \mathcal{N} = 3$ (MIMO), $\mathcal{M} = 3, \mathcal{N} = 1$ (MISO), and $\mathcal{M} = 1, \mathcal{N} = 1$ (SISO), respectively. These results strongly support the application of MIMO in FSO communication systems as a promising technique to improve the link performance. Other outcomes, particularly for the asymptotic result at high SNR, can be noticed similar to Fig. 8.

To ascertain the aperture averaging effect together with MIMO scheme, the variation of the average BER for OOK is given in Fig. 11 depending on both receiver aperture diameter and MIMO scheme. On setting two different receiver aperture diameters ($D_G = 1$ mm and $D_G = 30$ cm) for each MIMO scheme, it is observed that $D_G = 30$ cm yields better BER
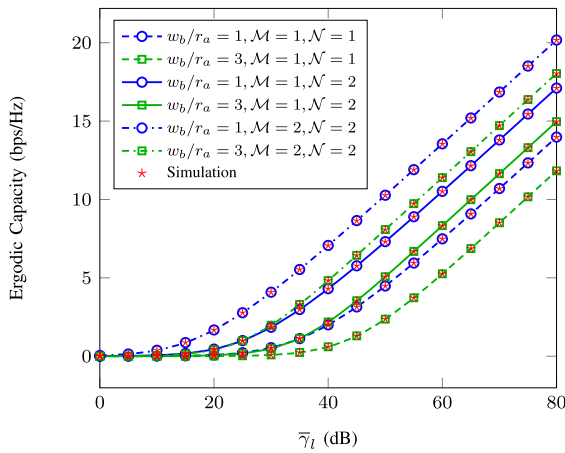
Fig. 12. Ergodic capacity of uplink against the average SNR for various values of beam waist, transmitter and receiver aperture number.
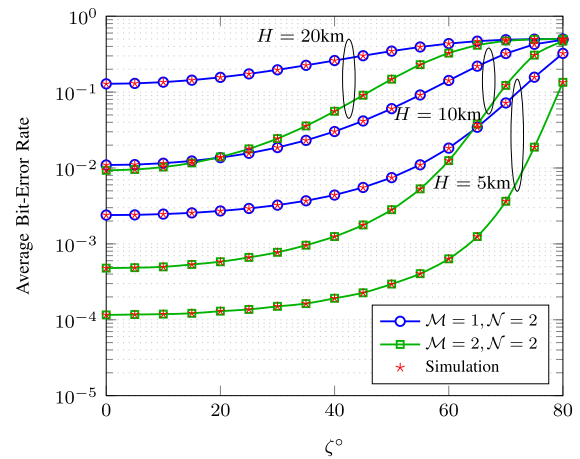

Fig. 13. Uplink average BER performance against the zenith angle for various values of air platform altitude, transmitter and receiver aperture number.

performance. Moreover, aperture averaging has more impact on reducing the average BER in single-input single-output (SISO) configuration. The reason for the lower improvement in the average BER performance for MIMO compared to SISO could be that MIMO application has already caused a reduction, which limits the aperture averaging impact in this scenario.

Fig. 12 illustrates the ergodic capacity performance of FSO uplink with varying effects of the beam waist. Setting the number of transmitter and receiver apertures to $\mathcal{M} = 1, \mathcal{N} = 1$, $\mathcal{M} = 1, \mathcal{N} = 2$ and $\mathcal{M} = 2, \mathcal{N} = 2$ produces the ergodic capacity values of $\overline{C} \sim 1.29$, $\overline{C} \sim 3.53$ and $\overline{C} \sim 6.43$, respectively when beam waist is $\omega_b/r_a = 3$ and $\overline{\gamma}_l = 45$ dB. It can be observed from Fig. 12 that for higher number of apertures in MIMO scheme, the ergodic capacity gets better, especially for lower values of the beam waist. For instance, changing the normalized beam waist from $\omega_b/r_a = 3$ to $\omega_b/r_a = 1$ improves the ergodic capacity from $\overline{C} \sim 4.82$ bps/Hz to $\overline{C} \sim 7.06$ bps/Hz when the average SNR is $\overline{\gamma}_l = 40$ dB for $\mathcal{M} = 2, \mathcal{N} = 2$.

The positive effect of smaller zenith angle on the average BER for a ground-to-HAPS FSO uplink with MIMO scheme is depicted in Fig. 13. From Fig. 13, it can be seen that when HAPS hover at higher altitudes, the average BER performance is reduced. For instance, applying $\mathcal{M} = 1, \mathcal{N} = 2$ and setting the zenith angle as $\zeta = 60°$, an uplink from the ground station to a HAPS hovering at $H = 5$ km altitude has an average BER of $\overline{P}_e \sim 1.83 \times 10^{-2}$ then, the average BER becomes $\overline{P}_e \sim 4.35 \times 10^{-1}$ when HAPS ascends to $H = 20$ km altitude.

To reflect the impact of MIMO on the horizontal FSO link, Figs. 14 and 15 are plotted. Fig. 14 demonstrates the ergodic capacity improvement for horizontal FSO link when the number of receiver apertures is increased. For a single transmitter $\mathcal{M} = 1$ and average SNR $\overline{\gamma}_l = 50$ dB, the ergodic capacity increases from $\overline{C} \sim 1.69$ bps/Hz to $\overline{C} \sim 5.85$ bps/Hz when the number of receiver apertures is increased from $\mathcal{N} = 2$ to $\mathcal{N} = 6$. In Fig. 15, the benefit of both spatial diversity application and larger FoV on horizontal FSO link performance is illustrated. It is noted that the performance improvement becomes substantial with the increase of FoV together with the higher number of receiver apertures.
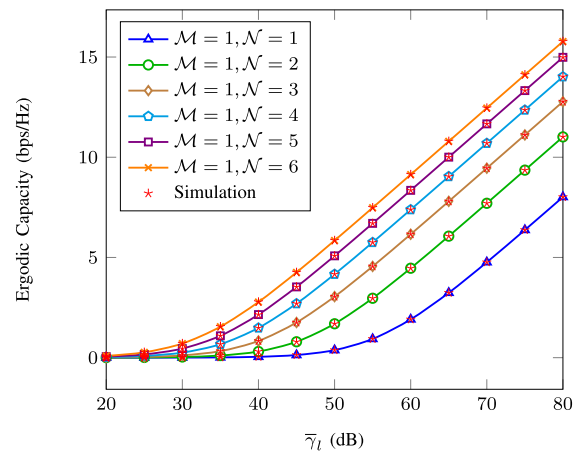

Fig. 14. Horizontal link ergodic capacity versus average SNR for different values of receiver aperture number.
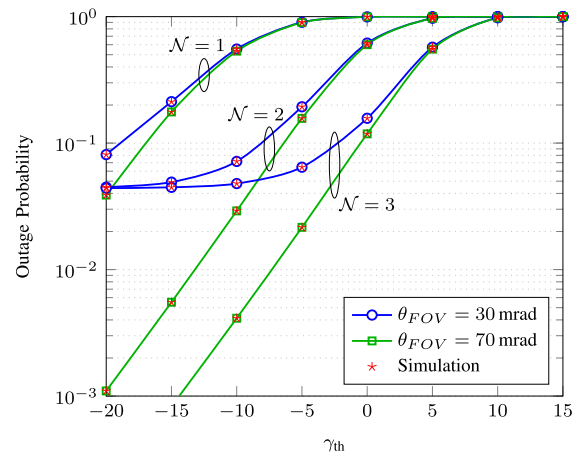

Fig. 15. Horizontal link outage performance versus threshold SNR for different values of FoV and receiver aperture number for $\mathcal{M} = 1$.

VI. CONCLUSION

In this study, we conducted a comprehensive analysis of the outage performance, the average BER, and the ergodic capacity HAPS-assisted MIMO FSO links. Our investigation thoroughly considered the effects of atmospheric turbulence, pointing errors, absorption- and scattering-induced attenuation, and AOA fluctuations. We observed a significant and undeniable benefit of MIMO application for all configurations of HAPS-based integrated MIMO FSO communication links. Our proposed model indicates that, given the challenges in implementing MIMO on HAPS, considering SIMO and MISO scenarios can be practical alternatives for improving performance. Consequently, our findings suggest potential opportunities for designing integrated ground-to-HAPS and HAPS-to-HAPS links, along with optimizing FSO communication system parameters. It should be noted that the HAPS-assisted FSO communication has enormous potential to continue to evolve, addressing current limitations and unlocking new capabilities for future communication networks. Design, deployment and optimization of HAPS, accurate channel modelling including all possible phenomena together with leveraging the machine learning (ML) and artificial intelligence (AI) technologies remain open for future research directions in terms of performance enhancement using HAPS as relay terminals.

APPENDIX A
DERIVATIONS OF THE CHANNEL PDF

Inserting (17) and (22) into (24)

$$f_{h_{ag}|\theta_d}(h_{ag}) = \int_{-\pi}^{\pi} \frac{\eta_s^2 h_{ag}^{\eta_s^2\xi(\varphi)-1}\left(\frac{\alpha_1\beta_1}{\mathcal{MN}}\right)^{\frac{\alpha_1+\beta_1}{2}}}{\pi q_H (A_0 h_{al}\cos\theta_d)^{\eta_s^2\xi(\varphi)}\Gamma(\alpha_1)\Gamma(\beta_1)}$$

$$\times \int_{\Delta}^{\infty} h_{at}^{\frac{\alpha_1+\beta_1}{2}-\eta_s^2\xi(\varphi)-1} K_{\alpha_1-\beta_1}\left(2\sqrt{\frac{\alpha_1\beta_1}{\mathcal{MN}}h_{at}}\right) dh_{at} d\varphi. \tag{A.1}$$

where $\Delta = h_{ag}/(A_0 h_{al}\cos\theta_d)$. According to (14) of [46], the modified Bessel function in (A.1) can be expressed as $K_v(x) = \frac{1}{2}\mathrm{G}_{0,2}^{2,0}\left[\frac{x^2}{4}\bigg|_{v/2,-v/2}^{-}\right]$. Then, (A.1) becomes

$$f_{h_{ag}|\theta_d}(h_{ag}) = \int_{-\pi}^{\pi} \frac{\eta_s^2 h_{ag}^{\eta_s^2\xi(\varphi)-1}\left(\frac{\alpha_1\beta_1}{\mathcal{MN}}\right)^{\frac{\alpha_1+\beta_1}{2}}}{2\pi q_H (A_0 h_{al}\cos\theta_d)^{\eta_s^2\xi(\varphi)}\Gamma(\alpha_1)\Gamma(\beta_1)}$$

$$\times \int_{\Delta}^{\infty} h_{at}^{\frac{\alpha_1+\beta_1}{2}-\eta_s^2\xi(\varphi)-1}\mathrm{G}_{0,2}^{2,0}\left[\frac{\alpha_1\beta_1 h_{at}}{\mathcal{MN}}\bigg|_{\frac{\alpha_1-\beta_1}{2},\frac{\beta_1-\alpha_1}{2}}^{-}\right] dh_{at} d\varphi. \tag{A.2}$$

Using Eq. (07.34.21.0085.01) of [47], h_{at} dependent integration in (A.2) will be obtained as

$$f_{h_{ag}|\theta_d}(h_{ag}) = \frac{\eta_s^2}{2\pi q_H \Gamma(\alpha_1)\Gamma(\beta_1) h_{ag}}$$

$$\times \int_{-\pi}^{\pi} \mathrm{G}_{1,3}^{3,0}\left[\frac{\alpha_1\beta_1 h_{ag}}{\mathcal{MN} A_0 h_{al}\cos\theta_d}\bigg|_{\alpha_1,\beta_1,\eta_s^2\xi(\varphi)}^{1+\eta_s^2\xi(\varphi)}\right] d\varphi. \tag{A.3}$$

Then, the resulting PDF of the combined channel state for FSO communication link can be computed through the following equation

$$f_h(h) = \int_0^{\theta_{FOV}} f_{h_{ag}|\theta_d}(h) f_{\theta_d}(\theta_d) d\theta_d + \delta(h) \int_{\theta_{FOV}}^{\infty} f_{\theta_d}(\theta_d) d\theta_d, \tag{A.4}$$

where $\delta(.)$ is the Dirac-delta function. Substituting (12) and (A.3) into (A.4) yields

$$f_h(h) = \frac{\eta_s^2}{2\pi q_H \Gamma(\alpha_1)\Gamma(\beta_1)\sigma_0^2 h}$$

$$\times \int_{-\pi}^{\pi} \mathrm{G}_{1,3}^{3,0}\left[\frac{\alpha_1\beta_1 h}{\mathcal{MN} A_0 h_{al}\cos\theta_d}\bigg|_{\alpha_1,\beta_1,\eta_s^2\xi(\varphi)}^{1+\eta_s^2\xi(\varphi)}\right] d\varphi$$

$$\times \int_0^{\theta_{FOV}} \theta_d \exp\left(-\frac{\theta_d^2}{2\sigma_0^2}\right) d\theta_d + \frac{\delta(h)}{\sigma_0^2}\int_{\theta_{FOV}}^{\infty}\theta_d \exp\left(-\frac{\theta_d^2}{2\sigma_0^2}\right) d\theta_d. \tag{A.5}$$

The last integral in (A.5) can be solved with the help of [41, Eq. (3.381-9)] that is expressed by

$$\int_u^{\infty} t^m \exp(-\beta t^r) dt = \frac{\Gamma(v,\beta u^r)}{r\beta^v}, \tag{A.6}$$

where $\Gamma(a,x) = \int_x^{\infty} e^{-s}s^{a-1}ds$ is the upper incomplete gamma function, $v = \frac{m+1}{r}$, $\mathrm{Re}\,r > 0$ and $\mathrm{Re}\,\beta > 0$. Utilizing (A.6) and using the property $\Gamma(1,b) = \exp(-b)$, (A.5) becomes

$$f_h(h) = \frac{\eta_s^2}{2\pi q_H \Gamma(\alpha_1)\Gamma(\beta_1)\sigma_0^2 h}$$

$$\times \int_{-\pi}^{\pi} \mathrm{G}_{1,3}^{3,0}\left[\frac{\alpha_1\beta_1 h}{\mathcal{MN} A_0 h_{al}\cos\theta_d}\bigg|_{\alpha_1,\beta_1,\eta_s^2\xi(\varphi)}^{1+\eta_s^2\xi(\varphi)}\right] d\varphi$$

$$\times \int_0^{\theta_{FOV}} \theta_d \exp\left(-\frac{\theta_d^2}{2\sigma_0^2}\right) d\theta_d + \delta(h)\exp\left(-\frac{\theta_{FOV}^2}{2\sigma_0^2}\right). \tag{A.7}$$

In (A.7), to drive θ_d dependent integral, we will use small angle approximation $\cos\theta_d \simeq 1$ that is also used in [5]. Then, (A.7) simplifies to

$$f_h(h) = \frac{\eta_s^2}{2\pi q_H \Gamma(\alpha_1)\Gamma(\beta_1)\sigma_0^2 h}$$

$$\times \int_{-\pi}^{\pi} \mathrm{G}_{1,3}^{3,0}\left[\frac{\alpha_1\beta_1 h}{\mathcal{MN} A_0 h_{al}}\bigg|_{\alpha_1,\beta_1,\eta_s^2\xi(\varphi)}^{1+\eta_s^2\xi(\varphi)}\right] d\varphi$$

$$\times \int_0^{\theta_{FOV}} \theta_d \exp\left(-\frac{\theta_d^2}{2\sigma_0^2}\right) d\theta_d + \delta(h) \exp\left(-\frac{\theta_{FOV}^2}{2\sigma_0^2}\right).$$

(A.8)

The θ_d dependent integral can be solved by using [41, Eq. (3.381-8)] which is formulated as

$$\int_0^u x^m \exp(-\beta x^n) dx = \frac{\gamma(v, \beta u^n)}{n\beta^v},$$

(A.9)

where $\gamma(a, x) = \int_0^x e^{-t} t^{a-1} dt$ is the lower incomplete gamma function, $v = \frac{m+1}{n}$, $u > 0$, $\mathrm{Re}\, v > 0$, $\mathrm{Re}\, n > 0$ and $\mathrm{Re}\, \beta > 0$. Applying (A.9) to (A.8), the PDF of the combined channel state can be determined as indicated in (25).

APPENDIX B
DERIVATIONS OF THE SNR CDF

By substituting (26) into (27), the CDF can be expressed as

$$F_\gamma(\gamma) = \frac{\eta_s^2 \left(1 - \exp\left(-\frac{\theta_{FOV}^2}{2\sigma_0^2}\right)\right)}{4\pi q_H \Gamma(\alpha_1)\Gamma(\beta_1)}$$

$$\times \int_{-\pi}^{\pi} \int_0^{\gamma} x^{-1} \mathrm{G}_{1,3}^{3,0}\left[\frac{\alpha_1\beta_1}{\mathcal{MN}A_0 h_{al}}\sqrt{\frac{x}{\gamma}}\,\bigg|\,\begin{matrix}1+\eta_s^2\xi(\varphi)\\ \alpha_1, \beta_1, \eta_s^2\xi(\varphi)\end{matrix}\right] dx\, d\varphi$$

$$+ \exp\left(-\frac{\theta_{FOV}^2}{2\sigma_0^2}\right) \int_0^{\gamma} \frac{1}{2\sqrt{\gamma x}} \delta\left(\sqrt{\frac{x}{\gamma}}\right) dx.$$

(B.1)

Using the RV transformation $t = \sqrt{x/\gamma}$ in the second part of (B.1), the SNR CDF reduces to

$$F_\gamma(\gamma) = \frac{\eta_s^2 \left(1 - \exp\left(-\frac{\theta_{FOV}^2}{2\sigma_0^2}\right)\right)}{4\pi q_H \Gamma(\alpha_1)\Gamma(\beta_1)}$$

$$\times \int_{-\pi}^{\pi} \int_0^{\gamma} x^{-1} \mathrm{G}_{1,3}^{3,0}\left[\frac{\alpha_1\beta_1}{\mathcal{MN}A_0 h_{al}}\sqrt{\frac{x}{\gamma}}\,\bigg|\,\begin{matrix}1+\eta_s^2\xi(\varphi)\\ \alpha_1, \beta_1, \eta_s^2\xi(\varphi)\end{matrix}\right] dx\, d\varphi$$

$$+ \exp\left(-\frac{\theta_{FOV}^2}{2\sigma_0^2}\right) \int_0^{\sqrt{\gamma/\overline{\gamma}}} \delta(t) dt.$$

(B.2)

Now, applying [44, Eq. (2.24.2/2)], we derive the CDF expression of the end-to-end SNR as given in (28).

APPENDIX C
DERIVATIONS OF THE AVERAGE BER

Substituting (26) into (37) and expressing erfc(·) through the Meijer's G function $\mathrm{erfc}(\sqrt{\gamma}/2) = 1/\sqrt{\pi}\,\mathrm{G}_{1,2}^{2,0}\left[\frac{\gamma}{4}\,\big|\,\begin{matrix}1\\0,\frac{1}{2}\end{matrix}\right]$ [44, Eq. (8.4.14/2)], the average BER in Eq.(37) can be re-written as

$$\overline{P}_e = \frac{\eta_s^2 \left(1 - \exp\left(-\frac{\theta_{FOV}^2}{2\sigma_0^2}\right)\right)}{8\pi^{\frac{3}{2}} q_H \Gamma(\alpha_1)\Gamma(\beta_1)} \int_{-\pi}^{\pi} \int_0^{\infty} x^{-1} \mathrm{G}_{1,2}^{2,0}\left[\frac{x}{4}\,\bigg|\,\begin{matrix}1\\0,\frac{1}{2}\end{matrix}\right]$$

$$\times \mathrm{G}_{1,3}^{3,0}\left[\frac{\alpha_1\beta_1}{\mathcal{MN}A_0 h_{al}}\sqrt{\frac{x}{\gamma}}\,\bigg|\,\begin{matrix}1+\eta_s^2\xi(\varphi)\\ \alpha_1, \beta_1, \eta_s^2\xi(\varphi)\end{matrix}\right] dx\, d\varphi$$

$$+ \frac{\exp\left(-\frac{\theta_{FOV}^2}{2\sigma_0^2}\right)}{2} \int_0^{\infty} \mathrm{erfc}\left(\frac{\sqrt{x}}{2}\right) \frac{1}{2\sqrt{\overline{\gamma}x}} \delta\left(\sqrt{\frac{x}{\overline{\gamma}}}\right) dx.$$

(C.1)

Integrating the first integral of (C.1) by applying [44, Eq. (2.24.1/1)] and utilizing the RV transformation $t = \sqrt{x/\overline{\gamma}}$ in the second integral with some algebraic manipulations, the average BER can be derived as shown by (38).

REFERENCES

[1] M. Sharma, D. Chadha, and V. Chandra, "High-altitude platform for free-space optical communication: Performance evaluation and reliability analysis," *J. Opt. Commun. Netw.*, vol. 8, no. 8, pp. 600–609, 2016.

[2] L. Yang, J. Yuan, X. Liu, and M. O. Hasna, "On the performance of LAP-based multiple-hop RF/FSO systems," *IEEE Trans. Aerosp. Electron. Syst.*, vol. 55, no. 1, pp. 499–505, Feb. 2019.

[3] Y. Zeng, R. Zhang, and T. J. Lim, "Wireless communications with unmanned aerial vehicles: Opportunities and challenges," *IEEE Commun. Mag.*, vol. 54, no. 5, pp. 36–42, May 2016.

[4] M. Mozaffari, W. Saad, M. Bennis, Y.-H. Nam, and M. Debbah, "A tutorial on UAVs for wireless networks: Applications, challenges, and open problems," *IEEE Commun. Surv. Tut.*, vol. 21, no. 3, pp. 2334–2360, Third Quarter, 2019.

[5] H. Safi, A. Dargahi, J. Cheng, and M. Safari, "Analytical channel model and link design optimization for ground-to-HAP free-space optical communications," *IEEE/OSA J. Lightw. Technol.*, vol. 38, no. 18, pp. 5036–5047, Sep. 2020.

[6] W. Guo, Y. Zhan, T. A. Tsiftsis, and L. Yang, "Performance and channel modeling optimization for hovering UAV-assisted FSO links," *IEEE/OSA J. Lightw. Technol.*, vol. 40, no. 15, pp. 4999–5012, Aug. 2022.

[7] Y. Ata and M.-S. Alouini, "HAPS based FSO links performance analysis and improvement with adaptive optics correction," *IEEE Trans. Wireless Commun.*, vol. 22, no. 7, pp. 4916–4929, Jul. 2023.

[8] O. B. Yahia, E. Erdogan, G. K. Kurt, I. Altunbas, and H. Yanikomeroglu, "HAPS selection for hybrid RF/FSO satellite networks," *IEEE Trans. Aerosp. Electron. Syst.*, vol. 58, no. 4, pp. 2855–2867, Aug. 2022.

[9] R. Samy, H. -C. Yang, T. Rakia, and M. -S. Alouini, "Space-air-Ground FSO networks for high-throughput satellite communications," *IEEE Commun. Mag.*, vol. 60, no. 12, pp. 82–87, Mar. 2023.

[10] R. K. Tyson, "Bit-error rate for free-space adaptive optics laser communications," *J. Opt. Soc. Amer. A*, vol. 19, no. 4, pp. 753–758, 2002.

[11] E. J. Lee and V. W. S. Chan, "Part 1: Optical communication over the clear turbulent atmospheric channel using diversity," *IEEE J. Sel. Areas Commun.*, vol. 22, no. 9, pp. 1896–1906, Nov. 2004.

[12] W. O. Popoola, Z. Ghassemlooy, J. I. H. Allen, E. Leitgeb, and S. Gao, "Free-space optical communication employing subcarrier modulation and spatial diversity in atmospheric turbulence channel," *IET Optoelectron.*, vol. 2, no. 1, pp. 16–23, 2008.

[13] N. Cvijetic, S. G. Wilson, and M. Brandt-Pearce, "Performance bounds for free-space optical MIMO systems with APD receivers in atmospheric turbulence," *IEEE J. Sel. Areas Commun.*, vol. 26, no. 3, pp. 3–12, Apr. 2008.

[14] Z. Wang, W.-D. Zhong, S. Fu, and C. Lin, "Performance comparison of different modulation formats over free-space optical (FSO) turbulence links with space diversity reception technique," *IEEE Photon. J.*, vol. 1, no. 6, pp. 277–285, Dec. 2009.

[15] E. Bayaki, R. Schober, and R. K. Mallik, "Performance analysis of MIMO free-space optical systems in gamma-gamma fading," *IEEE Trans. Commun.*, vol. 57, no. 11, pp. 3415–3424, Nov. 2009.

[16] X. Song and J. Cheng, "Subcarrier intensity modulated MIMO optical communications in atmospheric turbulence," *J. Opt. Commun. Netw.*, vol. 5, no. 9, pp. 1001–1009, 2013.

[17] A. Kamboj, R. K. Mallik, M. Agrawal, and R. Schober, "Diversity combining in FSO systems in presence of non-Gaussian noise," in *Proc. IEEE Int. Conf. Signal Process. Commun.*, 2012, pp. 1–5.

[18] D. Chen, G. Huang, G. Liu, and Y. Lei, "Performance of adaptive subcarrier modulated MIMO wireless optical communications in Malaga turbulence," *Opt. Commun.*, vol. 435, pp. 265–270, 2019.

[19] P. Kaur, V. K. Jain, and S. Kar, "Performance analysis of FSO array receivers in presence of atmospheric turbulence," *IEEE Photon. Technol. Lett.*, vol. 26, no. 12, pp. 1165–1168, Jun. 2014.

[20] P. Kaur, V. K. Jain, and S. Kar, "Performance analysis of free space optical links using multi-input multi-output and aperture averaging in presence of turbulence and various weather conditions," *IET Commun.*, vol. 9, no. 8, pp. 1104–1109, 2015.

[21] A. Garcia-Zambrana, C. Castillo-Vazquez, and B. Castillo-Vazquez, "Outage performance of MIMO FSO links over strong turbulence and misalignment fading channels," *Opt. Exp.*, vol. 19, no. 14, pp. 13480–13496, 2011.

[22] G. K. Varotsos, H. E. Nistazakis, C. K. Volos, and G. S. Tombras, "FSO links with diversity pointing errors and temporal broadening of the pulses over weak to strong atmospheric turbulence channels," *Optik*, vol. 127, no. 6, pp. 3402–3409, 2016.

[23] M. Al-Nahhal, T. Ismail, H. Selmy, and M. M. Elmesalawy, "BPSK based SIM-FSO communication system with SIMO over log-normal atmospheric turbulence with pointing errors," in *Proc. IEEE 19th Int. Conf. Transp. Opt. Netw.*, 2017, pp. 1–4.

[24] M. R. Bhatnagar and Z. Ghassemlooy, "Performance analysis of gamma–gamma fading FSO MIMO links with pointing errors," *J. Lightw. Technol.*, vol. 34, no. 9, pp. 2158–2169, May 2016.

[25] T. Ismail, E. Leitgeb, Z. Ghassemlooy, and M. Al-Nahhal, "Performance improvement of FSO system using multi-pulse pulse position modulation and SIMO under atmospheric turbulence conditions and with pointing errors," *IET Netw.*, vol. 7, no. 4, pp. 165–172, 2018.

[26] G. K. Varotsos, H. E. Nistazakis, W. Gappmair, G. G. Sandalidis, and G. S. Tombras, "SIMO subcarrier PSK FSO links with phase noise and non-zero boresight pointing errors over turbulence channels," *IET Commun.*, vol. 13, no. 7, pp. 831–836, 2019.

[27] H. S. Khallaf, K. Kato, E. M. Mohamed, S. M. Sait, H. Yanikomeroglu, and M Uysal, "Composite fading model for aerial MIMO FSO links in the presence of atmospheric turbulence and pointing errors," *IEEE Wireless Commun. Lett.*, vol. 10, no. 6, pp. 1295–1299, Jun. 2021, doi: 10.1109/LWC.2021.3064832.

[28] M. T. Dabiri, M. Rezaee, I. S. Ansari, and V. Yazdanian, "Channel modeling for UAV-Based optical wireless links with nonzero boresight pointing errors," *IEEE Trans. Veh. Technol.*, vol. 69, no. 12, pp. 14238–14246, Dec. 2020, doi: 10.1109/TVT.2020.3037308.

[29] M. T. Dabiri, S. M. S. Sadough, and M. A. Khalighi, "Channel modeling and parameter optimization for hovering UAV-based free-space optical links," *IEEE J. Sel. Areas Commun.*, vol. 36, no. 9, pp. 2104–2113, Sep. 2018.

[30] J.-Y. Wang, Y. Ma, R.-R. Lu, J.-B. Wang, M. Lin, and J. Cheng, "Hovering UAV-based FSO communications: Channel modelling, performance analysis, and parameter optimization," *IEEE J. Sel. Areas Commun.*, vol. 39, no. 10, pp. 2946–2959, Oct. 2021.

[31] N. T. Nguyen, M. Q. Vu, H. T. Pham, B. H. Dang, and T. D. Ngoc, "Performance enhancement of HAP-based relaying M-PPM FSO system using spatial diversity and heterodyne detection receiver," *J. Opt. Commun.*, vol. 42, no. 1, pp. 111–120, 2021.

[32] E. T. Michailidis, P. S. Bithas, N. Nomikos, D. Vouyioukas, and A. G. Kanatas, "Outage probability analysis in multi-user FSO/RF and UAV-enabled MIMO communication networks," *Phys. Commun.*, vol. 49, 2021, Art. no. 101475.

[33] S. J. Kim and S. K. Han, "Efficient MIMO configuration for bi-directional vertical FSO link with multiple beam induced pointing error," *Sensors*, vol. 22, no. 23, 2022, Art. no. 9147.

[34] L. C. Andrews and R. L. Phillips, *Laser Beam Propagation Through Random Media*, 2nd ed. Bellingham, WA, USA: SPIE, 2005.

[35] M. C. Al Naboulsi, H. Sizun, and F. de Fornel, "Fog attenuation prediction for optical and infrared waves," *Opt. Eng.*, vol. 43, no. 2, pp. 319–329, 2004.

[36] W. Gappmair, S. Hranilovic, and E. Leitgeb, "OOK performance for terrestrial FSO links in turbulent atmosphere with pointing errors modeled by Hoyt distributions," *IEEE Commun. Lett.*, vol. 15, no. 8, pp. 875–877, Aug. 2011.

[37] A. A. Farid and S. Hranilovic, "Outage capacity optimization for free-space optical links with pointing errors," *IEEE/OSA J. Lightw. Technol.*, vol. 25, no. 7, pp. 1702–1710, Jul. 2007.

[38] W. Gappmair, S. Hranilovic, and E. Leitgeb, "Performance of PPM on terrestrial FSO links with turbulence and pointing errors," *IEEE Commun. Lett.*, vol. 14, no. 5, pp. 468–470, May 2010.

[39] D. A. Luong and A. T. Pham, "Average capacity of MIMO free-space optical gamma-gamma fading channel," in *Proc. IEEE Int. Conf. Commun.*, 2014, pp. 3354–3358.

[40] N. D. Chatzidiamantis and G. K. Karagiannidis, "On the distribution of the sum of gamma-gamma variates and applications in RF and optical wireless communications," *IEEE Trans. Commun.*, vol. 59, no. 5, pp. 1298–1308, May 2011.

[41] I. S. Gradshteyn and I. M. Ryzhik, *Table of Integrals, Series, and Products*, 8th ed. London, U.K.: Academic (Press Inc), 2014.

[42] A. Kilbas and M. Saigo, *H-Transforms: Theory and Applications*. 1st ed. Boca Raton, FL, USA: CRC Press, 2004.

[43] A. Lapidoth, S. M. Moser, and M. A. Wigger, "On the capacity of free-space optical intensity channels," *IEEE Trans. Inf. Theory*, vol. 55, no. 10, pp. 4449–4461, Oct. 2009.

[44] A. P. Prudnikov, Y. A. Brychkov, and O. I. Marichev, *Integrals and Series*, vol. 3, Boca Raton, FL, USA: CRC Press, 1999.

[45] A. Gupta, D. Dhawan, and N. Gupta, "Review on UAV-based FSO links: Recent advances, challenges, and performance metrics," *Opt. Eng.*, vol. 63, no. 4, 2023, Art. no. 041204.

[46] V. Adamchik and O. Marichev, "The algorithm for calculating integrals of hypergeometric type functions and its realization in REDUCE system," in *Proc. Int. Symp. Symbolic Algebr. Comput.*, 1990, pp. 212–224.

[47] *Wolfram. Inc.*, "The wolfram functions site," 2023. Accessed: Jan. 10, 2023. [Online]. Available: https://functions.wolfram.com